Computational homogenization simulation on steel reinforced resin used in the injected bolted connections

Xin, Haohui; Nijgh, Martin; Veljkovic, Milan

DOI
10.1016/j.compstruct.2018.11.069

Publication date
2019

Document Version
Final published version

Published in
Composite Structures

Citation (APA)
Xin, H., Nijgh, M., & Veljkovic, M. (2019). Computational homogenization simulation on steel reinforced resin used in the injected bolted connections. *Composite Structures*, *210*, 942-957. https://doi.org/10.1016/j.compstruct.2018.11.069

Composite Structures 210 (2019) 942–957

Contents lists available at ScienceDirect

Composite Structures

journal homepage: www.elsevier.com/locate/compstruct

Computational homogenization simulation on steel reinforced resin used in the injected bolted connections

Haohui Xin*, Martin Nijgh, Milan Veljkovic

Faculty of Civil Engineering and Geosciences, Delft University of Technology, Delft, the Netherlands

ARTICLE INFO

Keywords:
Steel reinforced resin
Linear Drucker-Prager plastic model
Finite element simulation
Computational homogenization

ABSTRACT

In this paper, compressive material tests on unconfined/confined resin and steel reinforced resin were experimentally evaluated in order to validate the numerical results. The uniaxial model which combines damage mechanics and Ramberg-Osgood relationship is proposed in this paper to describe the uniaxial compressive behaviour of resin and steel reinforced resin. Numerical homogenization is conducted to predict the tensile and shear behaviour of steel reinforced resin after validated by compressive material test results. The friction angle β, the ratio of the yield stress in triaxial tension to the yield stress in triaxial compression K, and the dilation angle ψ of the linear drucker-prager plastic model are obtained based on experiments and numerical homogenization simulation. The confinement effects on resin and steel reinforced resin could be effectively simulated by combing above parameters and uniaxial compressive model. Finite element simulations on unconfined/ confined resin and steel reinforced resin material tests were conducted to validate the material parameters proposed in this paper. A good agreement is observed, indicating the model and parameters proposed in this paper could be effectively used in the finite element simulation of injected bolts.

1. Introduction

Injected bolts are regarded as a suitable alternative for a renovation of fitted bolts, riveted or preloaded connections of large span structures [1–3]. As shown in Fig. 1, a hole is included in the head of the bolt in order to inject with resin/steel reinforced resin. After injection and curing of the resin, the connection is slip resistant. Recently, the injected material, epoxy resin is modified at TU Delft by adding the steel shots [4]. The shots serve as a reinforcement while epoxy resin serving as a matrix. The increase of compressive strength and the expected improvement of creep characteristics of the reinforced injected materials, especially in a bolt hole serving as nature confinement environment, will improve the performance of connections exposed to monotonic and cyclic loading.

In addition to experimental research, numerical simulations could play an important role in the qualification and certification of short- and long-term behaviour of injection bolts. The material models of resin/steel reinforced resin should be investigated before conducting finite element simulation on injection bolts. However, the material behaviour of reinforced resin depends on the type of resin, type of the reinforcing material and the volume fraction. It is important to adopt a multi-scale analysis to determine the mechanical properties of the steel-reinforced resin. Numerical homogenization methods [5], which could accurately consider the geometry and spatial distribution of the phases, and also could precisely estimate the propagation of damage to accurately predict the failure strength, is considered to be an effective modeling tool to analyze steel reinforced resin. Fish et al. [6–8] successfully use the statistically computational homogenization methods to predict the macroscopic behaviour of different materials. Xin et al. [9–12] adopted a multi-scale analysis in determining mechanical properties of pultruded GFRP laminates and successfully predict the mechanical behaviour of a pultruded GFRP bridge deck. Gonzalez and LLorca [13] analyzed the mechanical response of a unidirectional FRP subjected to transverse compression. Vaughan and McCarthy [14] investigate the effect of fiber-matrix debonding and thermal residual stress on the transverse damage behavior of unidirectional FRP.

Computational homogenization methods of fine scale models provide a pathway to use high fidelity models to predict macroscopic mechanical responses of steel reinforced resin. However, the high fidelity numerical homogenization methods are reported computationally expensive [7,8,15–17]. The hierarchical strategy, where experimental results and high fidelity model (HFM) are employed to train a low fidelity model (LFM) and to supplement experimental database is adapted to model the material behavior of steel reinforced resin [7]. The performance of the steel reinforced resin is effectively predicted by an elaborate but computationally inexpensive low fidelity model

* Corresponding author.
E-mail address: H.Xin@tudelft.nl (H. Xin).

https://doi.org/10.1016/j.compstruct.2018.11.069
Received 3 October 2018; Received in revised form 20 November 2018; Accepted 26 November 2018
Available online 26 November 2018

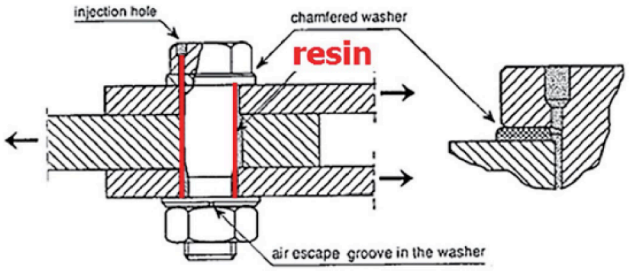

(a) Injection bolts [3]

(b) steel reinforced resin [4]

Fig. 1. Schematic of injected bolts and steel reinforced resin.

identified by a more fundamental but computationally taxing high fidelity model, which has been calibrated to the experimental results.

In this paper, compressive material tests on unconfined/confined resin and steel reinforced resin were experimentally evaluated. The uniaxial model which combines damage mechanics and the Ramberg-Osgood relationship is proposed to describe the uniaxial compressive behavior of resin and steel reinforced resin. First-order numerical homogenization is employed as high fidelity model, where combined non-linear isotropic/kinematic cyclic hardening model is employed to define the steel plasticity, the linear Drucker-Prager plastic criterion was used to simulate resin damage, and the cohesive surfaces reflecting the relationship between traction and displacement at the interface. The linear Drucker-Prager plastic model is used as a low fidelity model. The friction angle β, the ratio of the yield stress in triaxial tension to the yield stress in triaxial compression K, and the dilation angle ψ of the linear Drucker-Prager plastic model are obtained based on experiments and numerical homogenization simulation. Finite element simulations on unconfined/ confined resin and steel reinforced resin material tests were conducted to validate the proposed material parameters. This research may contribute to numerical simulation and practical design of injection bolts.

2. Computational homogenization

2.1. Computational homogenization and periodic boundary condition

The link between micro-scale and macro-scale behavior could be established based on Hill-Mandel computational Homogenization method. The macro-scale Cauchy stress σ_{ij} is obtained by averaging the microscale Cauchy stress,$\widetilde{\sigma}_{ij}$, in the unit cell domain, expressed as below [5]:

$$\sigma_{ij} = \frac{1}{|\Theta|}\int_{\Theta} \widetilde{\sigma}_{ij} d\Theta \tag{1}$$

where: σ_{ij} is the macro-scale Cauchy stress, $\widetilde{\sigma}_{ij}$is the micro-scale Cauchy stress, Θ is the domain of the unit cell. The unit cell problem could be solved for the leading order translation-free micro-scale displacement. The micro-scale displacement $u_i^f(x, y)$ is expressed in the following form [5]:

$$u_i^f(x, y) = \varepsilon_{ij}^c y_j + u_i^{(1)}(x, y) \tag{2}$$

where: x is the macro-scale position vector in the macro-scale domain, y is the micro-scale position vector in the unit cell domain; ε_{ij}^c is the strain tensors in the macro-scale domain, $u_i^{(1)}(x, y)$ is the perturbation displacement of the micro-scale.

If two nodes, M and S, located at the opposite faces of the unit cell, with M and S being the master and slave nodes respectively, the fine-scale displacement at the two nodes is given as [5] Eq. (3) and Eq. (4) based on expression in Eq. (2).

$$u_i^f(x, y^M) = \varepsilon_{ij}^c y_j^M + u_i^{(1)}(x, y_j^M) \tag{3}$$

$$u_i^f(x, y^S) = \varepsilon_{ij}^c y_j^S + u_i^{(1)}(x, y_j^S) \tag{4}$$

where: y^M, and y^S are the fine-scale coordinates.

Considering the periodic boundary conditions [5] in the unit cell domain gives:

$$u_i^{(1)}(x, y_j^M) = u_i^{(1)}(x, y_j^S) \tag{5}$$

Thus, above two equations yield to the following relation [5]:

$$u_i^f(x, y_j^M) - u_i^f(x, y_j^S) = \varepsilon_{ij}^c(y_j^M - y_j^S) \tag{6}$$

This could be implemented by so-called "*mixed boundary conditions*" via constraint equations, is expressed by the following equations [5,17]:

$$\int_{\partial\Theta_Y} (u_i^f(x, y) - \varepsilon_{ik}^c y_k) N_j^{\Theta} d\gamma_Y = 0 \tag{7}$$

$$|u_i^f(x, y) - \varepsilon_{ik}^c y_k| \, N_j^{\Theta} \leqslant Tol \tag{8}$$

where: N_j^{Θ} is the unit normal to the unit cell boundary $\partial\Theta_y$.

2.2. Material constitutive law

The microscale material model generally include individual submaterials components constitutive law and steel-resin interface behavior. Each constitutive model is detailed explained as below section.

2.2.1. Steel

The combined non-linear isotropic/kinematic cyclic hardening model is employed to define the steel plasticity [18]. The yield surface generally consists of two components, (i) a nonlinear kinematic hardening component, which describe the translation of the yield surface in stress space through the back-stress; and (ii) an isotropic hardening component, which describe the change of the equivalent stress defining the size of the yield surface as a function of plastic deformation. As is shown in Fig. 2, the pressure-independent yield surface is defined as Eq.

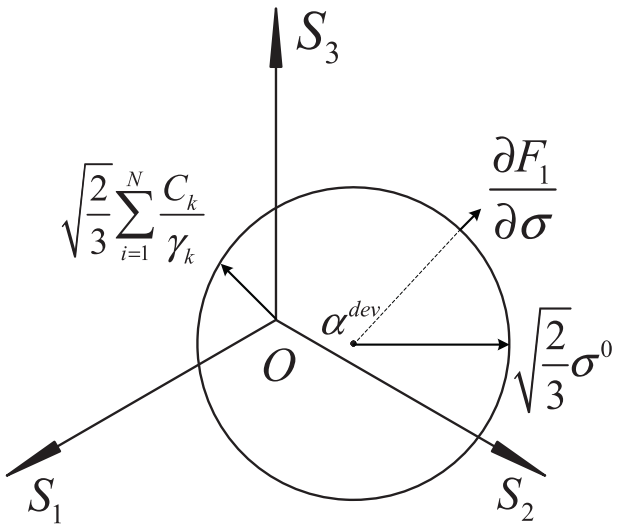

Fig. 2. Hardening of the nonlinear isotropic/kinematic model in π-plane.

(9).

$$F_1 = f(\sigma - \alpha) - \sigma^0 = 0 \tag{9}$$

where σ^0 is the yield stress and $f(\sigma - \alpha)$ is the equivalent Mises stress with respect to the back stress α.

The equivalent Mises stress is shown below:

$$f(\sigma - \alpha) = \sqrt{\frac{3}{2}(S_{ij} - \alpha_{ij}^{dev}) : (S_{ij} - \alpha_{ij}^{dev})} \tag{10}$$

where S_{ij} is deviatoric stress tensor, α_{ij}^{dev} is the deviatoric part of the backstress tensor. The associated plastic flow rule is used in the kinematic hardening models, given by:

$$\dot{\varepsilon}_{ij}^{p} = \dot{\lambda}\frac{\partial F_1}{\partial \sigma_{ij}} \tag{11}$$

where ε_{ij}^{p} is the plastic strain and $\lambda$is the equivalent plastic strain. The evolution of the equivalent plastic strain is obtained by assuming equivalent plastic work between isotropic plasticity and combined isotropic/kinematic plasticity same as below:

$$\sigma^0\sqrt{\frac{2}{3}\dot{\varepsilon}_{ij}^{p} : \dot{\varepsilon}_{ij}^{p}} = \sigma_{ij} : \dot{\varepsilon}_{ij}^{p} \tag{12}$$

The non-linear kinematic/isotropic hardening is employed to describe the translation of the yield surface in stress space. The kinematic hardening is specified by half-cycle input material data. For each input material data point (σ_i, ε_i^{pl}) based on Eurocode EN 1993-1-1 [19], a value of backstress α_i is obtained from the input data as:

$$\alpha_i = \sigma_i - \sigma_i^0 \tag{13}$$

where σ_i^0 is the user-defined size of the yield surface at the corresponding plastic strain for the isotropic hardening component. Integration of the backstress evolution laws over a half cycle yields the expression:

$$\alpha = \sum_{k=1}^{N}\left[\frac{C_k}{\gamma_k}(1 - e^{-\gamma_k \varepsilon_i^{pl}})\right] \tag{14}$$

where N is the number of back stresses, C_k and γ_k are material parameters and calibrated through material data by Eq. (13).

2.2.2. Resin

The epoxy resin is assumed to behave as isotropic material. The plastic behavior of resin was assumed to be governed by the linear Drucker-Prager model. The yield surface of the linear Drucker-Prager model [18] is given in Eq. (15).

$$F_2 = t - p\tan\beta - d = 0 \tag{15}$$

$$t = \frac{1}{2}q\left[1 + \frac{1}{K} - \left(1 - \frac{1}{K}\right)\left(\frac{r}{q}\right)^3\right] \tag{16}$$

where β is the slope of the linear yield surface and is commonly referred as the friction angle of the material, d is the cohesion of the material, K is the ratio of the yield stress in triaxial tension to the yield stress in triaxial compression, and controls the dependence of the yield surface on the value of the intermediate principal stress. p is the hydrostatic stress:

$$p = -\frac{1}{3}\sigma_{ij}\delta_{ij} \tag{17}$$

q is the Mises equivalent stress:

$$q = \sqrt{\frac{3}{2}S_{ij}S_{ij}} \tag{18}$$

$r$is the third invariant of deviatoric stress:

$$r = \left(\frac{9}{2}S_{ij}\cdot S_{ij} : S_{ij}\right)^{1/3} \tag{19}$$

The cohesion d of the material is related to the input material data as:

(i) if hardening/softening is defined by the uniaxial compression yield stress σ_c:

$$d = (1 - \frac{1}{3}\tan\beta)\sigma_c \tag{20}$$

(ii) if hardening/softening is defined by the uniaxial tension yield stress σ_t:

$$d = (\frac{1}{K} + \frac{1}{3}\tan\beta)\sigma_t \tag{21}$$

(ii) if hardening/softening is defined by the uniaxial shear yield stress τ:

$$d = \frac{\sqrt{3}}{2}\tau(1 + \frac{1}{K}) \tag{22}$$

The flow potential of linnear drucker-prager model is choosen as below equations.

$$G = \mathrm{t} - p\tan\psi \tag{23}$$

where ψ is the dilation angle.

2.2.3. Steel-Resin interface

The cohesive surfaces reflecting the relationship between traction and displacement at the interface were employed to simulate the steel-

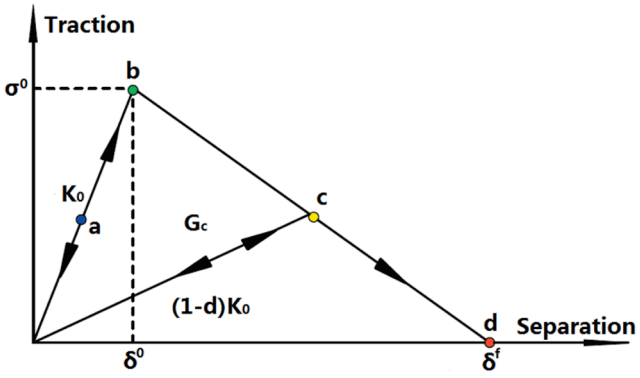

(a) Bilinear constitutive law

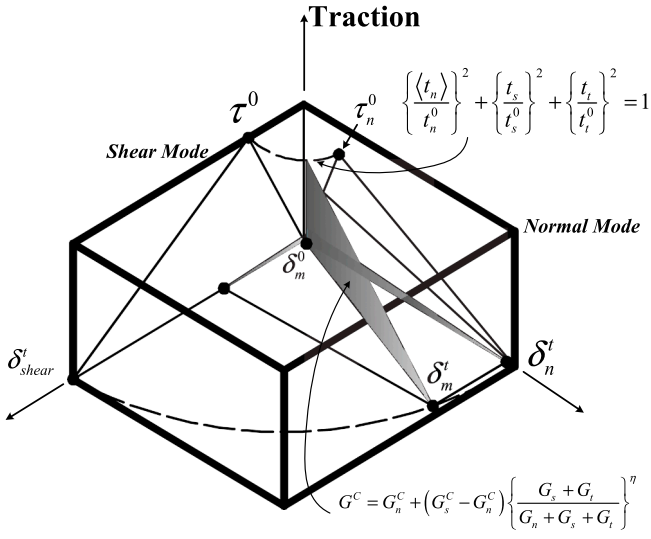

(b) The mixed-mode response of cohesive elements

Fig. 3. Illustration of interface behavior [12]

resin interface. As is shown in Fig. (3-a), the bilinear traction-separation model, which assumed to be linear elastic (point "*a*") followed by the damage initiation (point "*b*"), the evolution of damage (point "*c*"), and finally the fully damaged state (point "*d*"), is employed in this paper. In the elastic stage, the traction increased linearly along the displacement with an initial slope of K_0. At point "*b*", the damage of cohesive element is initiated. The cohesive element is always subjected to complicated loading condition; the quadratic stress failure criterion [18] is used to evaluate the initial damage, as is shown in Fig. (3-b).

$$\left\{\frac{\langle t_n\rangle}{t_n^0}\right\}^2+\left\{\frac{t_s}{t_s^0}\right\}^2+\left\{\frac{t_t}{t_t^0}\right\}^2=1 \tag{24}$$

where: t_n, t_s and t_t are traction components related to pure modes *I, II* and *III*, t_n^0, $t_s^0$and t_t^0 are the interfacial strength of pure modes *I, II* and *III*.

In the damage evolution period, the interfacial stiffness degraded from initial K_0 to (1-*d*) K_0, where *d* is a damaged variable. The Benzeggagh-Kenane fracture criterion (BK Law) [18,20] described in Eq. (25) is particularly used to predict damage propagation of mixed-mode loadings in terms of the critical fracture energies during deformation purely along the first and the second shear directions are the same.

$$G^C=G_n^C+(G_s^C-G_n^C)\left\{\frac{G_s+G_t}{G_n+G_s+G_t}\right\}^{\eta} \tag{25}$$

where: G_n, G_s, and G_t are the corresponding energy release rates under pure modes *I, II,* and *III*, the additional subscript "*C*" denotes critical case, which can be determined based on a standard fracture toughness test and η is a material parameter.

2.3. Matching Mohr-Coulomb parameters to the Drucker-Prager model

Sometimes, experimental data are not directly available to get the triaxial parameters of resin and steel reinforced resin. In this case, a simple way to proceed is to match the Mohr-Coulomb parameters to the Drucker-Prager model. The Mohr-Coulomb failure model is based on plotting Mohr's circle for states of stress at failure in the plane of the maximum and minimum principal stresses [18]. The linear Drucker-Prager flow potential defines the plastic strain increment as:

$$d\varepsilon^{pl}=d\tilde{\varepsilon}^{pl}\frac{1}{1-\tan\psi/3}\frac{\partial(t-p\tan\psi)}{\partial\sigma} \tag{26}$$

where: $d\tilde{\varepsilon}^{pl}$ is the equivalent plastic strain increment. Due to match the behavior in one plane, K is assumed to be 1. Then:

$$d\varepsilon^{pl}=d\tilde{\varepsilon}^{pl}\frac{1}{1-\tan\psi/3}\left(\frac{\partial q}{\partial\sigma}-\tan\psi\frac{\partial p}{\partial\sigma}\right) \tag{27}$$

Writing this expression in terms of principal stresses provides:

$$d\varepsilon_1^{pl}=d\tilde{\varepsilon}^{pl}\frac{1}{1-\tan\psi/3}\left(\frac{1}{2q}(2\sigma_1-\sigma_2-\sigma_3)+\frac{1}{3}\tan\psi\right) \tag{28}$$

Assume plain strain is in the 11-direction. At limit load, we have $d\varepsilon_1^{pl}=0$. Then, above equation provides below relationship:

$$\sigma_1=\frac{1}{2}(\sigma_2+\sigma_3)-\frac{1}{3}\tan\psi q \tag{29}$$

Then, the Drucker-Prager yield surface can be written in terms of σ_2 and σ_3 as:

$$\frac{9-\tan\beta\tan\psi}{2\sqrt{3(9-\tan^2\psi)}}(\sigma_2-\sigma_3)+\frac{1}{2}\tan\beta(\sigma_2+\sigma_3)\text{ - d}=0 \tag{30}$$

The Mohr-Coulomb yield surface in the 2–3 principal stress plane is

$$(\sigma_2-\sigma_3)+\sin\phi(\sigma_2+\sigma_3)\text{ - 2c}\cos\phi=0 \tag{31}$$

where: ϕ is friction angle of Mohr-Coulomb model, c is the cohesion of Mohr-Coulomb model.

By comparison [18],

$$\sin\phi=\frac{\tan\beta\sqrt{3(9-\tan^2\psi)}}{9-\tan\beta\tan\psi} \tag{32}$$

$$c=\frac{1}{\cos\phi}\frac{\sqrt{3(9-\tan^2\psi)}}{9-\tan\beta\tan\psi}d \tag{33}$$

Consider the two extreme cases of plastic flow definition: associated flow, $\psi=\beta$, and nondilatant flow $\psi=0$.

(i) For associated flow:

$$\tan\beta=\frac{\sqrt{3}\sin\phi}{\sqrt{1+\frac{1}{3}\sin^2\phi}} \tag{34}$$

$$\frac{d}{c}=\frac{\sqrt{3}\cos\phi}{\sqrt{1+\frac{1}{3}\sin^2\phi}} \tag{35}$$

(ii) For nondilatant flow:

$$\tan\beta=\sqrt{3}\sin\phi \tag{36}$$

$$\frac{d}{c}=\sqrt{3}\cos\phi \tag{37}$$

The parameters of Mohr-Coulomb yield surface could be determined from its tensile and compressive strengths, σ_t and σ_c, expressions as follows:

$$\sigma_t=2c\frac{\cos\phi}{1+\sin\phi} \tag{38}$$

$$\sigma_c=2c\frac{\cos\phi}{1-\sin\phi} \tag{39}$$

By combing Eqs. (20)–(22), (32), (33) and (38), (39), the ratio of the yield stress in triaxial tension to the yield stress in triaxial compression K is expressed as Eq. (40). The value of K in the linear Drucker-Prager model is restricted to K ≥ 0.778 for the yield surface to remain convex.

$$K=\min\left(\frac{3\text{ - }\sin\phi}{3+\sin\phi},0.778\right) \tag{40}$$

3. Experimental results and discussion

3.1. Specimens and material tests

The epoxy resin used in the tests is made of RenGel SW 404 with hardener HY 2404 in the room temperature. Reinforcing steel particles were chosen as steel shot S330 with nominal diameter 0.84 mm. Compression testes on both unconfined and confined conditions are carried out. As is shown in Figs. 4 and 5, the dimension of the unconfined specimen is Φ26mm × 50 mm. The nominal dimension of the confined specimen is Φ22mm × 22 mm, confined by S235 steel tube with a dimension of Φ30mm × 50 mm × 4 mm and loaded by a S355 steel cylinder with a dimension of Φ22mm × 40 mm. Five specimens of each type, totally 20 specimens, were prepared and tested in order to investigate the compressive behavior of resin and steel reinforced resin. The load is applied with a displacement speed of 0.01 mm/s. Two GS-551 linear variable displacement transformers (LVDTs) were employed to measure the axial deformation of the specimens.

3.2. Experimental results

3.2.1. Unconfined specimens

For nominal stress $\bar{\sigma}$ and nominal strain $\bar{\varepsilon}$, the original dimensions of the specimen are employed. However, length and cross-sectional area change in plastic region. True stress σ and true strain ε are used for the accurate definition of the plastic behaviour of ductile materials by

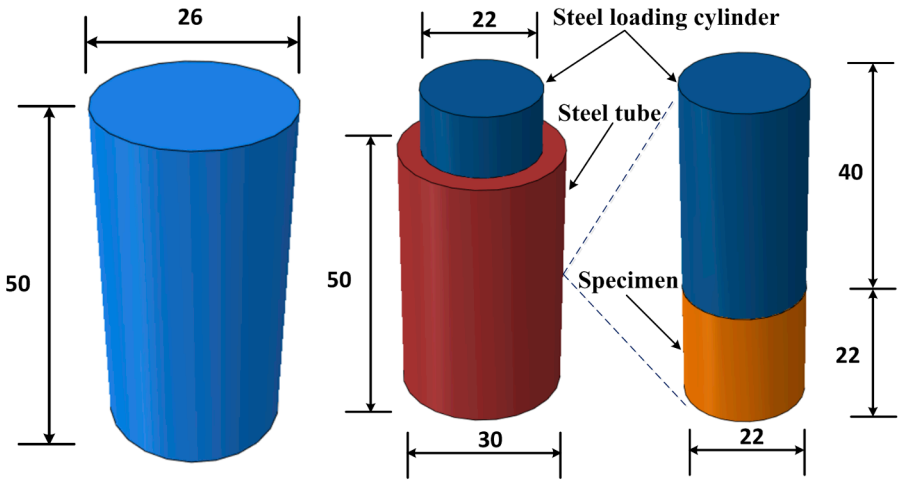

Fig. 4. Schematic of unconfined/confined specimens.

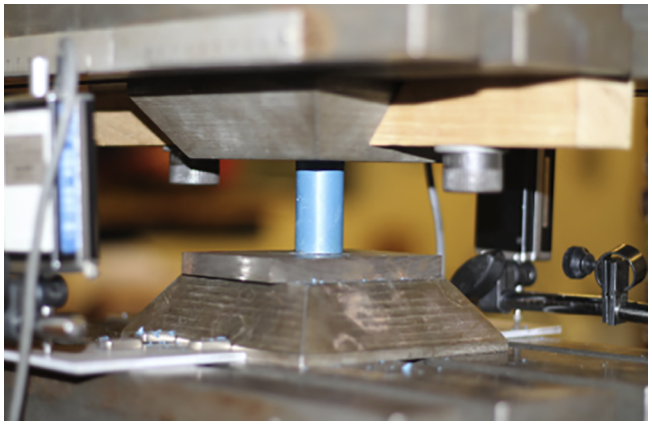

Fig. 5. Experimental set-up [1]

considering the actual dimensions. True stress σ is the force divided by the actual area. The true strain ε is a change in length with respect to the instant length. Due to large deformation of specimens, the nominal stress $\bar{\sigma}$ and nominal strain $\bar{\varepsilon}$ were converted to true stress σ and true strain ε based on Eqs. (41)–(44).

For compression:

$$\varepsilon = -\ln(1-\bar{\varepsilon}) \tag{41}$$

$$\sigma = \bar{\sigma}(1-\bar{\varepsilon}) \tag{42}$$

For tension:

$$\varepsilon = \ln(1+\bar{\varepsilon}) \tag{43}$$

$$\sigma = \bar{\sigma}(1+\bar{\varepsilon}) \tag{44}$$

The compressive results of unconfined resin and steel reinforced resin specimens are summarized in Tables 1–4. Based on nominal stress and strain, the average elastic modulus $\bar{E}$of resin and steel reinforced resin is 5.64 Gpa and 15.70 Gpa respectively, while the average ultimate strength $\bar{\sigma}^{u}$of resin and steel reinforced resin is 169.8Mpa and 120.30 Mpa respectively. Based on true stress and strain, the average elastic modulus E of resin and steel reinforced resin is 5.53 Gpa and 15.29 Gpa respectively, while the average ultimate strength σ^{u} of resin and steel reinforced resin is 140.7 Mpa and 119.43 Mpa respectively. It is noted that the true ultimate strength of unconfined resin is 17.6% smaller than the nominal ultimate strength. Attention should be paid on

Table 1
Results of unconfined resin specimen from norminal stress/strain.

Specimen	Young's Modulus $\bar{E}$(GPa)	Ultimate Strength $\bar{\sigma}^{u}$(MPa)	Fracture initiation Strain $\bar{\varepsilon}_0^f$(%)	Fracture Strain $\bar{\varepsilon}_u^f$(%)
U-R-1	5.30	171.7	18.20	21.59
U-R-2	6.15	168.9	18.34	21.86
U-R-3	5.83	173.2	18.20	20.24
U-R-4	5.45	168.7	17.34	22.31
U-R-5	5.49	166.6	17.96	24.84
Average	5.64	169.8	18.01	22.17
S.D.	0.34	2.62	0.40	1.68

Table 2
Results of unconfined resin specimen from true stress/strain.

Specimen	Young's Modulus E(GPa)	Ultimate Strength σ^{u}(MPa)	Fracture initiation Strain ε_0^f(%)	Fracture Strain ε_u^f(%)
U-R-1	5.20	141.69	19.70	24.66
U-R-2	6.02	139.23	19.43	24.72
U-R-3	5.72	142.43	19.78	24.34
U-R-4	5.33	141.47	18.64	24.51
U-R-5	5.38	138.72	19.71	26.58
Average	5.53	140.71	19.45	24.96
S.D.	0.33	1.63	0.47	0.92

Table 3
Results of unconfined steel reinforced resin specimen from nominal stress/strain.

Specimen	Young's Modulus $\bar{E}$(GPa)	Ultimate Strength $\bar{\sigma}^{u}$(MPa)	Fracture initiation Strain $\bar{\varepsilon}_0^f$(%)	Fracture Strain $\bar{\varepsilon}_u^f$(%)
U-SR-1	15.90	117.97	0.97	3.86
U-SR-2	16.30	119.52	1.01	4.87
U-SR-3	15.50	124.13	0.94	3.97
U-SR-4	15.60	119.48	1.08	4.84
U-SR-5	15.10	122.14	1.03	4.98
Average	15.70	120.30	1.01	4.51
S.D.	0.41	2.72	0.054	0.54

Table 4
Results of unconfined steel reinforced resin specimen from true stress/ strain.

Specimen	Young's Modulus E(GPa)	Ultimate Strength σ^u(MPa)	Fracture initiation Strain ε_0^f(%)	Fracture Strain ε_u^f(%)
U-SR-1	15.63	116.74	0.98	3.90
U-SR-2	15.72	118.32	1.02	4.98
U-SR-3	15.03	122.88	1.01	4.12
U-SR-4	15.16	118.27	1.09	4.92
U-SR-5	14.91	120.92	1.02	5.18
Average	15.29	119.43	1.03	4.62
S.D.	0.36	2.45	0.04	0.57

large differences between nominal and true ultimate compressive strength of resin during finite element simulation. The stress-strain relationship of unconfined resin and steel reinforced resin specimens were shown in Figs. 6 and 7. The stress-strain curve of unconfined resin generally consisted of three stages: (i) the stress increased linearly with strain increasing; (ii) yielding occurred, the stress increased nonlinearly with strain increasing; (iii) fracture initiated when the load reached the peak, the stress decreased with the strain increasing. The stress-strain curve of unconfined steel reinforced resin generally included two stages: (i) the stress increased almost linearly with strain increasing; (ii) damage occurred when the maximum strength is reached, the stress decreased gradually with strain increasing.

The failure mode of resin and steel reinforced resin specimens were shown in Fig. 8. The longitudinal and diagonal cracks of resin initiated with the loading increasing. The final failure of resin occurred after the long cracks propagated through the whole specimen and the specimen was split into two parts. The diagonal cracks of steel reinforced specimens initiated on the bottom half specimens. The steel reinforced specimen failed when the diagonal cracks propagated to the bottom of the specimen.

The tensile tests of the same resin were conducted by Wedekamper in 2017 [21]. The stress-strain curve of unconfined resin is reproduced [21] and showed in Fig. 9. Based on nominal stress and strain, the average elastic modulus $\bar{E}$of resin is 5.14 Gpa and the average ultimate strength $\bar{\sigma}^u$of resin is 63.30 Mpa. Based on true stress and strain, the average elastic modulus E of resin 5.25 Gpa and the average ultimate strength σ^u of resin is 64.47 MPa. It indicated that the difference between tensile elastic modulus (5.25 GPa) and compressive elastic modulus (5.53 Gpa) is very small (See Table 5).

3.2.2. *Confined specimens*

The compressive elastic modulus of confined resin and steel reinforced resin specimens were summarized in Table 6. It is noted that the confined specimen is not loaded to completely failure and the ultimate strength of the confined specimen is not obtained. Based on nominal stress and strain, the average elastic modulus $\bar{E}$of confined resin and the steel reinforced resin is 7.32 Gpa and 18.40 Gpa

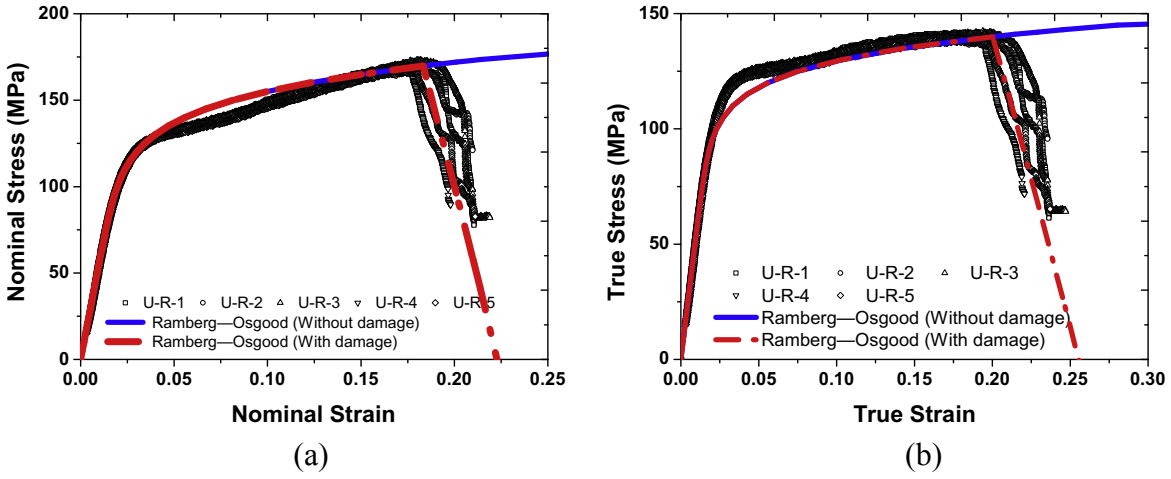

Fig. 6. Stress-strain relationship of unconfined resin specimens.

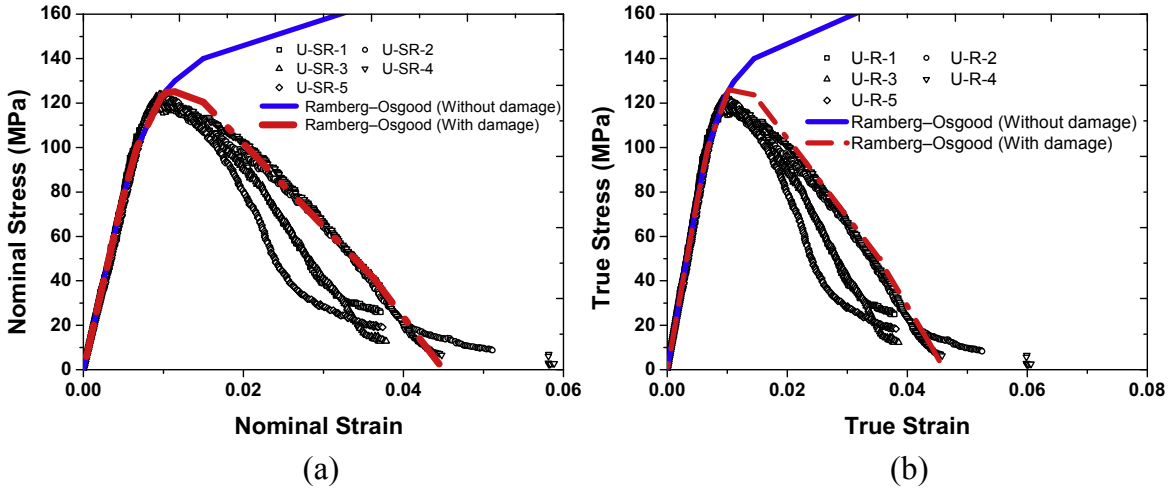

Fig. 7. Stress-strain relationship of unconfined steel reinforced resin specimens.

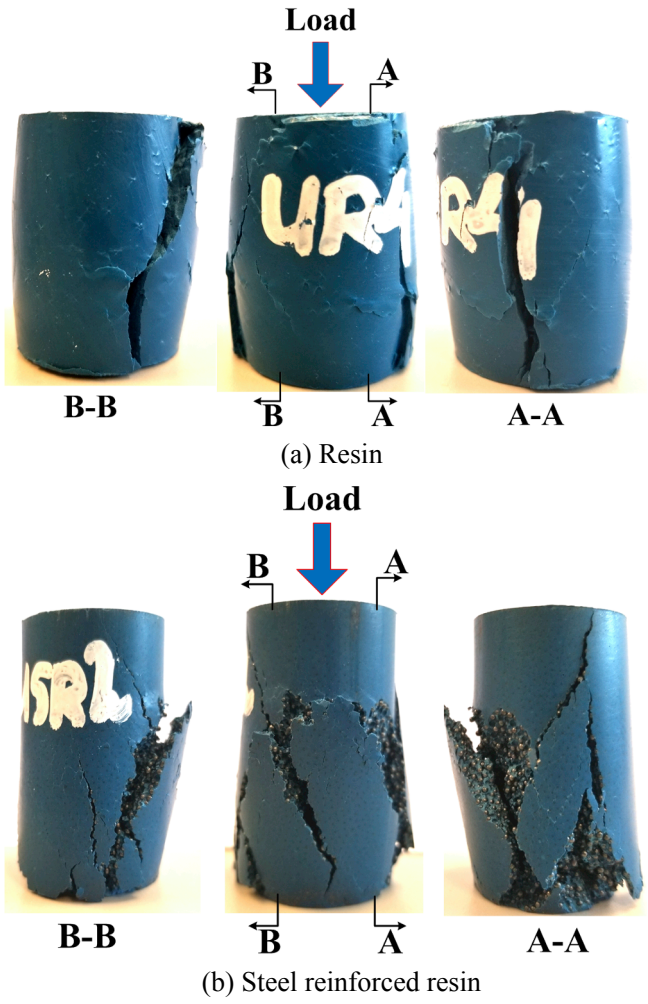

Fig. 8. Typical failure mode for resin and steel-reinforced resin.

respectively. Based on true stress and strain, the average elastic modulus E of resin and the steel reinforced resin is 7.09 Gpa and 18.09 Gpa respectively. The stress-strain relationship of confined resin and steel reinforced resin were shown in Figs. 10 and 11. The stress-strain curve of confined specimens consisted of two stages: (i) the stress increased linearly with strain increasing; (ii) yielding occurred, the stress increased nonlinearly with strain increasing. The non-linear branch of the

Table 5
Tensile elastic modulus and strength of resin.

Specimen	Nominal stress- nominal strain		True stress- true strain	
	$\bar{E}$(GPa)	$\bar{\sigma}^{u}$(MPa)	E(GPa)	σ^{u}(MPa)
U-R-T-1	5.13	59.41	5.27	60.24
U-R-T-2	5.37	61.91	5.52	62.78
U-R-T-3	5.08	66.35	5.18	67.42
U-R-T-4	5.30	65.56	5.37	66.35
U-R-T-5	4.82	63.26	4.91	65.56
Average	5.14	63.30	5.25	64.47
S.D.	0.21	2.81	0.22	2.92

Table 6
Elastic modulus of confined resin and steel reinforced resin.

Specimen	Confined Resin		Confined Steel Reinforced Resin	
	$\bar{E}$(GPa)	E(GPa)	$\bar{E}$(GPa)	E(GPa)
C-1	6.84	6.66	17.99	17.61
C-2	6.84	6.52	19.56	19.36
C-3	7.15	6.91	19.59	19.43
C-4	7.66	7.59	18.66	18.45
C-5	8.09	7.78	16.18	15.96
Average	7.32	7.09	18.40	18.16
S.D.	0.54	0.56	1.41	1.44

stress-strain curve of confined specimen is due to (i) the nonlinear behavior of material itself: the yield surface of resin and steel reinforced resin is hydrostatic pressure dependent; (ii) yielding of the confining steel tube: this leads to the situation where the resin is restrained less in lateral direction.

The deformation of the confined specimen is shown in Fig. 12. Obvious yielding is observed at the half bottom of the confined steel tube. The steel tube yielding of confined resin specimen is larger than the confined steel reinforced resin specimen, indicating that the Poisson's ratio of resin is larger than the steel reinforced resin. Small slip is observed at the bottom of the specimens. The slip of steel reinforced resin specimen is smaller than the confined resin specimen because steel reinforced resin has larger hardness but smaller Poisson's ratio.

3.2.3. Results discussion

The apparent Young's modulus increased 29.7% of confined resin specimens and increased 7.5% of confined steel reinforced resin specimens. An explanation for different increasement of elastic modulus is

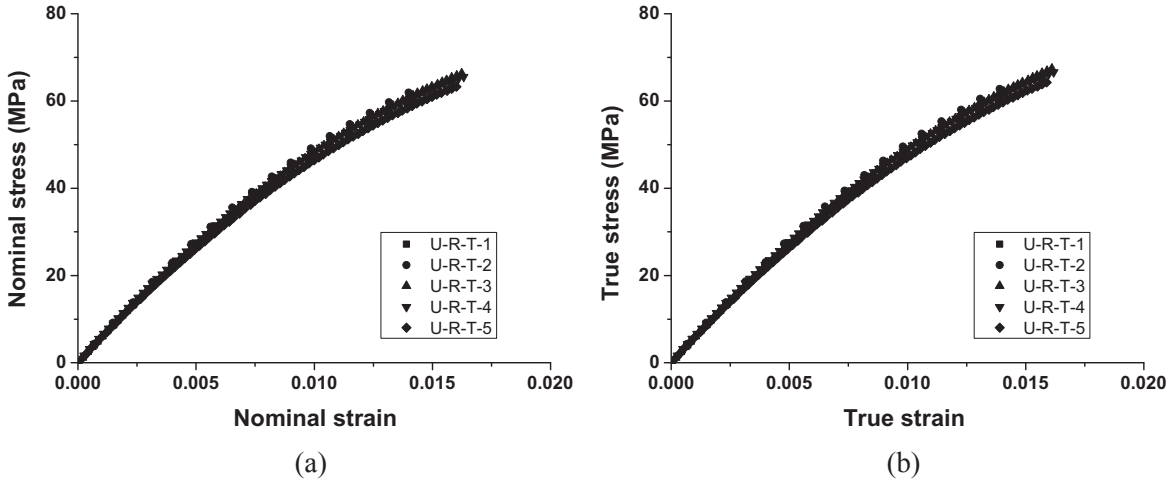

Fig. 9. Tensile stress-strain relationship of unconfined resin specimens [21].

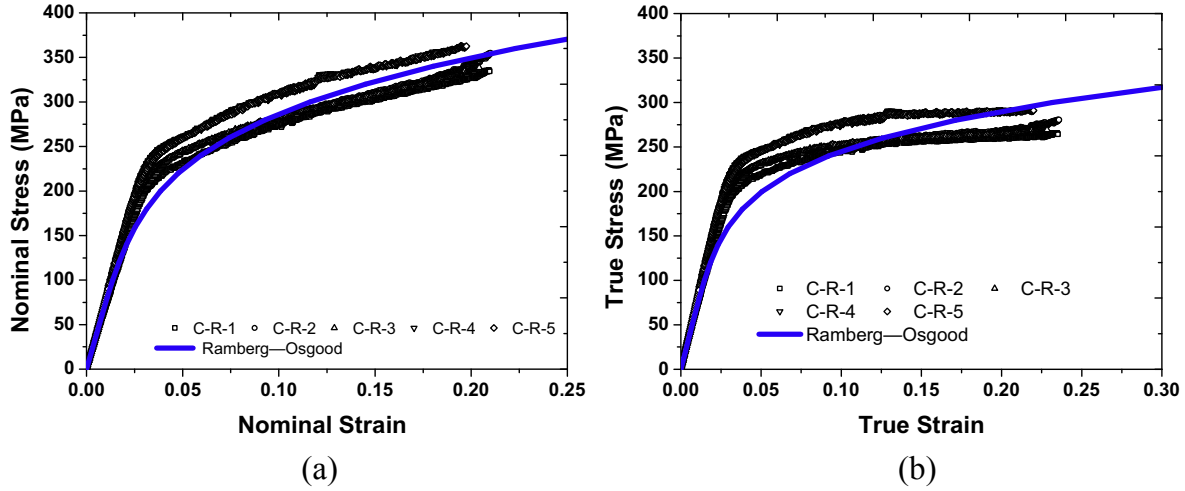

Fig. 10. Stress-strain relationship of confined resin specimens.

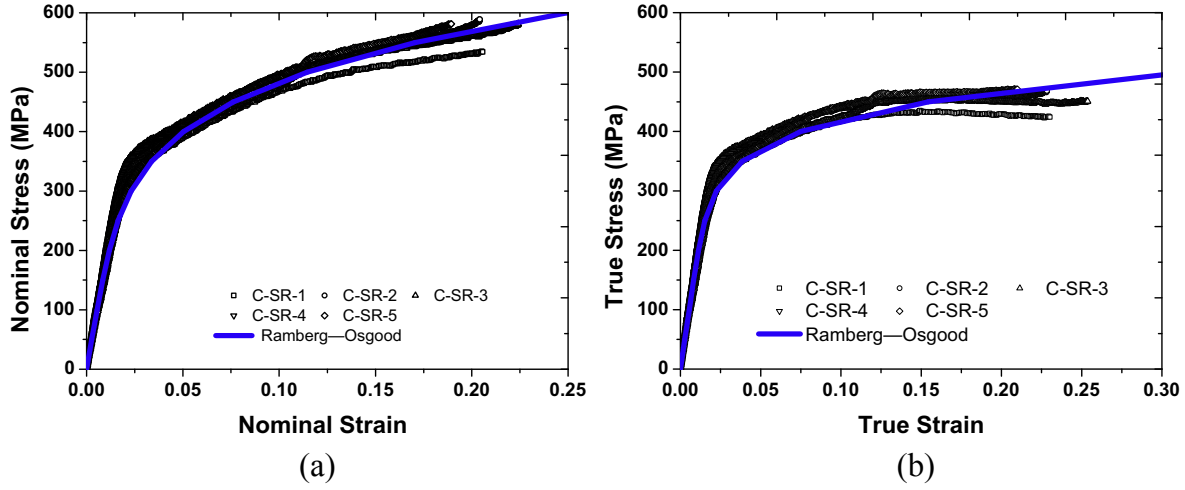

Fig. 11. Stress-strain relationship of confined steel reinforced resin specimens.

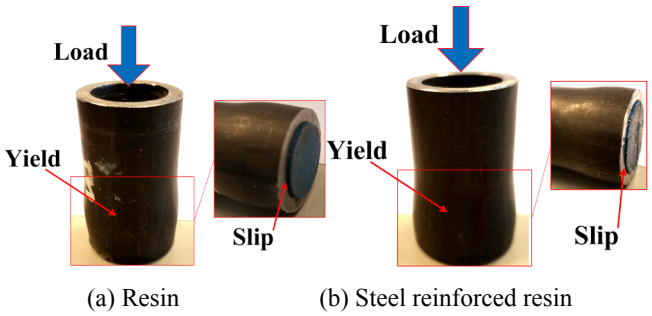

Fig. 12. Deformation of confined specimens.

that the Poisson's ratio of resin is larger than the steel reinforced resin. The strength of confined specimens is obviously increased. The yield strength increased by 95.6% of confined resin specimens, and the yield strength increased 189% of confined steel reinforced resin.

In the linear Drucker-Prager model, the confinement effects are controlled by the friction angle β, the ratio of the yield stress in triaxial tension to the yield stress in triaxial compression K, and the dilation angle ψ. The hardening/softening of the materials is controlled by the cohesion d related to the input uniaxial material data. The relationship between cohesion in the linear Drucker-Prager model and uniaxial compressive stress is shown in Eq. (20). This paper assumed that the uniaxial compressive behavior is described by combining the damage mechanics and Ramberg-Osgood Relationship [22], as shown in Eqs. (45) and (46).

$$\sigma = (1 - D)\sigma^{R-O}(\varepsilon) \tag{45}$$

$$\varepsilon = \frac{\sigma^{R-O}}{E} + K\left(\frac{\sigma^{R-O}}{E}\right)^{n} \tag{46}$$

where: D is damage variable.

The parameters of Ramberg-Osgood Relationship is fitted based on the experimental results before damage occurred. The fitted material parameters were listed in Table 7. The comparisons of stress-strain relationship from Ramberg-Osgood Relationship and experimental results is shown in Figs. 6, 7 and 10, 11. A good agreement is observed when no damage occurred. It is assumed that the fracture initiation occurred when the load reached the peak value. The damage variable is defined as below:

$$D = \begin{cases} 0 & \varepsilon < \varepsilon_0^f \\ \frac{\varepsilon - \varepsilon_0^f}{\varepsilon_u^f - \varepsilon_0^f} & \varepsilon \geqslant \varepsilon_0^f \end{cases} \tag{47}$$

where: ε_0^f is plastic strain at fracture initiation, ε_u^f is the plastic strain at the failure. The fracture initiation strain$\varepsilon_0^f$is assumed to be the

Table 7
Ramberg-Osgood Relationship Parameters of Resin and Steel-reinforced Resin.

Item		K	n	R^2
Unconfined Resin	Nominal Stress	6.07×10^{11}	8.27	0.98
	True Stress	1.62×10^{16}	10.62	0.95
Unconfined steel reinforced resin	Nominal Stress	7.81×10^{15}	8.83	0.99
	True Stress	4.43×10^{16}	9.15	0.94
Confined Resin	Nominal Stress	1.82×10^{5}	4.55	0.90
	True Stress	3.28×10^{6}	5.27	0.85
Confined steel reinforced resin	Nominal Stress	5.68×10^{6}	4.99	0.97
	True Stress	2.00×10^{11}	7.59	0.89

corresponding strain at the peak load while the failure strain is obtained by extended the softening stage. The values of ε_0^f and ε_u^f are listed in Tables 1–4 based on the experimental results. The comparisons between combined damage Ramberg-Osgood Relationship and experimental results is shown in Figs. 5–7. A good agreement is observed.

4. Numerical simulation of resin

4.1. Unconfined resin simulation

The unconfined resin compressive tests were simulated numerically using the commercial finite element software ABAQUS/Standard [18]. The specimen was simulated by solid element C3D8R. As is shown in Fig. 13, the vertical displacement UY of one end is fixed, and the vertical displacement load is applied on the other end of the specimen. Linear Drucker-Prager model described in Section 2.2.2 is employed to model the resin behavior. The true stress and strain relationship is calculated based on Eqs. (45), (46) and material parameters in Tables 2 and 7. The friction angle β, the ratio of the yield stress in triaxial tension to the yield stress in triaxial compression K, and the dilation angle ψ is calculated based on Eqs. (34)–(40). The resin material parameters of the the linear Drucker-Prager model are summarized in Table 8. It is noted that the yield compressive strength and yield tensile strength is used during calculating the material parameters of the the linear Drucker-Prager model. The nominal stress-strain of unconfined resin comparisons between finite element simulation and experimental results is shown in Fig. 14. A good agreement is observed, indicating the material model could effectively model the uniaxial loading of unconfined resin. The difference between "associated flow" material parameters and "nondilatant flow" parameters is very small on the uniaxial behavior of unconfined resin. Fig. 13 showed the principal plastic strain of resin. The maximum principal plastic strain is 0.01174 when the specimen is loaded to failure.

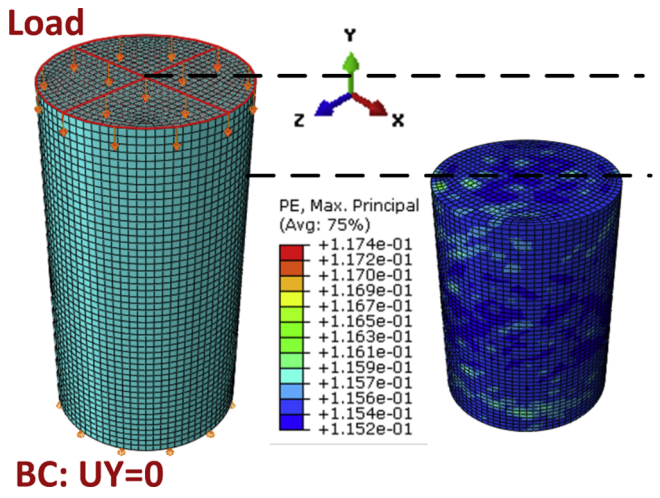

Fig. 13. Finite element model of unconfined resin specimen.

Table 8
Material Parameters of the linear Drucker-Prager model.

Material	Associated flow			Non-dilatant flow		
	β	K	ψ	β	K	ψ
Resin	12.16^0	0.92	12.16^0	12.18^0	1.00	0^0
Steel reinforced resin	49.80^0	0.78	49.80^0	52.04^0	1.00	0^0

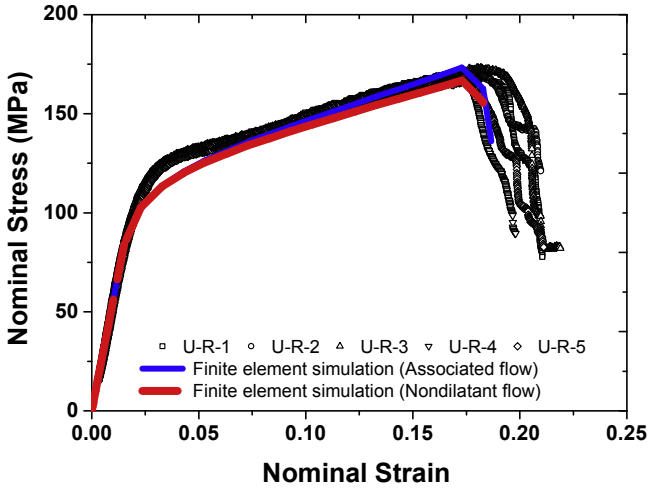

Fig. 14. Stress-strain relationship comparisons between FEM and experiments of unconfined resin.

4.2. Confined resin simulation

As is shown in Fig. 15, finite element model on confined resin tests was built to validate the efficiency of the the linear Drucker-Prager model when predicting resin behavior with confinement. Steel and resin were both simulated by solid element C3D8R [18]. All translation degrees of freedom on the bottom surface of the steel base was fixed, and vertical displacement is applied on the top surface of the steel cylinder to load the specimen until failure. Same material model and parameter used in the unconfined resin simulation is employed during modeling confined resin tests. The combined non-linear isotropic/kinematic cyclic hardening model, as described in Section 2.2.1, is employed to define the steel plasticity. The true stress and strain relationship is calculated based on Eurocode EN 1993-1-1 [19], where S235 grade steel is used in steel tube simulation and S355 grade steel is used in steel loading cylinder. The nominal stress-strain of confined resin comparisons between finite element simulation and experimental results is shown in Fig. 16. A good agreement is observed, indicating the Drucker-Prager model could effectively model the confinement effects

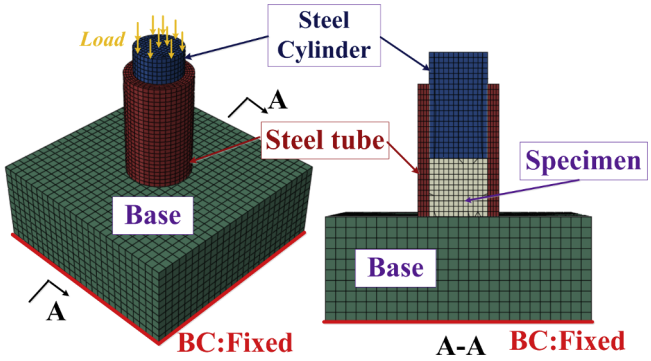

Fig. 15. Finite element model of confined material tests.

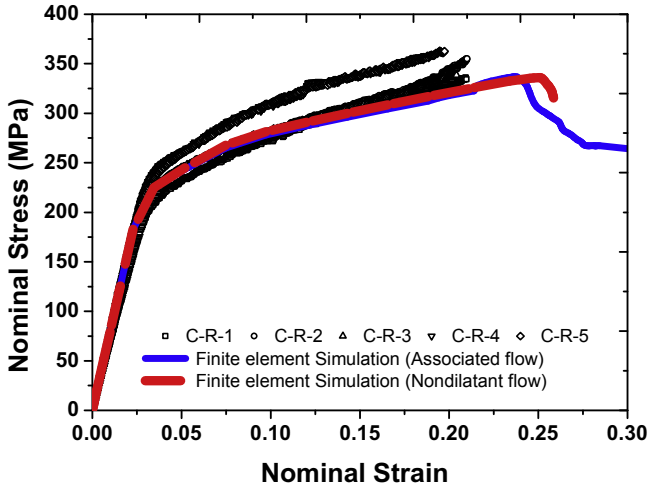

Fig. 16. Stress-strain relationship comparisons between FEM and experiments of confined resin.

of resin. The fracture initiation strain at the peak load from "non-dilatant flow" model is a little larger than it from "associated flow" model. Fig. 17 showed deformation comparisons of confined resin between FEM and experiments. A good agreement is observed.

5. Numerical simulation of steel reinforced resin

5.1. Unconfined steel reinforced resin

Due to the limit of the manufacture process of steel reinforced resin, it is difficult to make dog-shaped tensile specimens to obtain tensile behavior experimentally. The computational homogenization method provides an alternative way to obtain the tensile and shear behavior numerically after validating the multiscale model with compressive test results. The unit cell is shown in Fig. 18. Same material model and parameter used in Section 4 is employed to simulate the resin behavior in the computational homogenization modeling. S235 grade steel is employed to describe the behavior of steel shot based on Eurocode EN 1993-1-1[19]. The "mixed periodic boundary conditions" is applied to

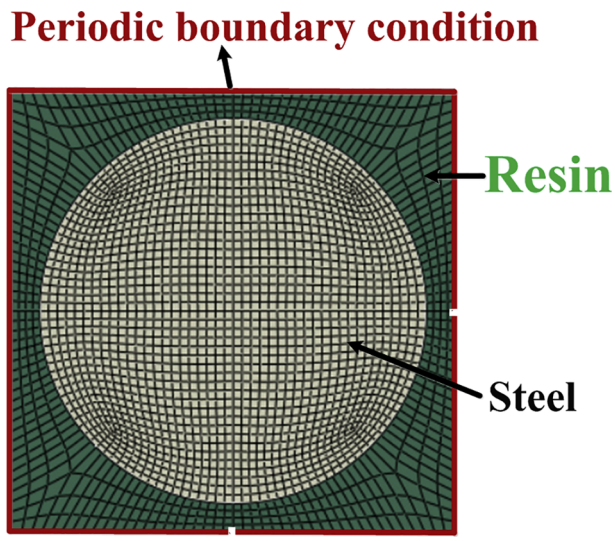

Fig. 18. Unit cell of steel reinforced resin.

the unit cell via constraint equations as expressed in Eqs. (7) and (8). Surface cohesive model, as detailed explained in Section 2.2.3, is used to describe the interface behavior between steel and resin.

The interface parameters are calibrated based on compressive test results. Below are the calibration procedures:

(i) as is shown in Eq. (48), the normal interface stiffness k_n is assumed to be the elastic modulus of resin $E_r$divide the interface thickness $t$while the shear interface stiffness $k_s$is assumed to be the shear modulus of resin $G_r$divide the interface thickness t. The thickness of the interface is calibrated by comparing the linear stage of the stress-strain curve between experimental and numerical homogenization. The interface thickness is determined to be 1%. The normal interface stiffness is calibrated as 5.53×10^5 N/mm^3, and the shear interface stiffness is calibrated as 2.01×10^5 N/mm^3.

$$k_n = \frac{E_r}{t},\ k_s = \frac{G_r}{t} \tag{48}$$

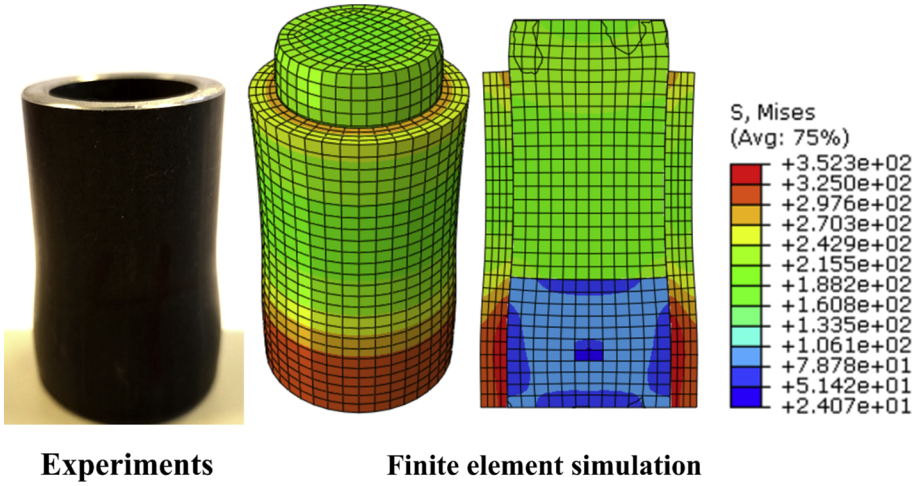

Fig. 17. Deformation comparisons between FEM and experiments of confined resin.

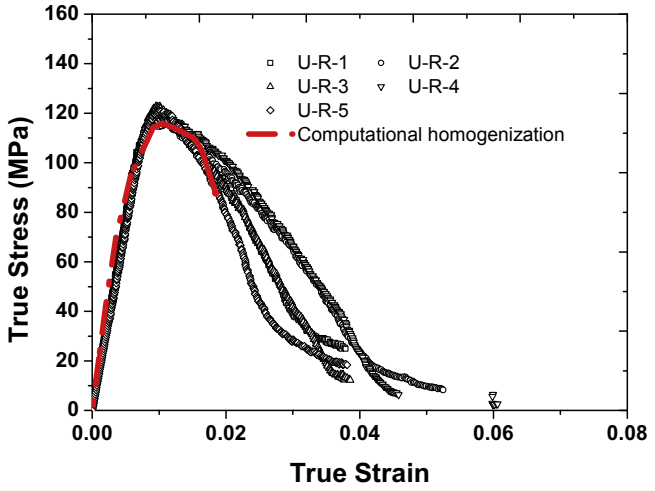

Fig. 19. Stress-strain relationship comparisons between numerical homogenization and experiments of unconfined steel reinforced resin.

(ii) The normal interface strength is assumed to be a parameter ξ_1 times the ultimate compressive strength σ_c^u of resin in Eq. (49). The shear interface strength is assumed to be a parameter ξ_2 times the ultimate shear strength $\tau^u$of resin in Eq. (50). The ultimate shear strength τ^u is further expressed as a function of compressive strength σ_c^u based on Eqs. (20) and (22). After comparing the peak compressive strength of steel reinforced resin between experimental and numerical homogenization, the parameter ξ_1 is determined as 0.29 and the parameter ξ_2 is determined as 0.57. The normal interface strength is calibrated as 40.8 Mpa. The shear interface strength is calibrated to be 41.5 Mpa.

$$t_n^0 = \xi_1 \sigma_c^u \tag{49}$$

$$t_s^0 = t_t^0 = \xi_2 \tau^u = \xi_2 \frac{2}{\sqrt{3}} \frac{1 - \tan\beta/2}{1 + 1/K} \sigma_c^u \tag{50}$$

(iii) The critical fracture energies are calibrated by comparing the softening stage of steel reinforced resin between experimental and numerical homogenization. The normal critical fracture energies G_n^c is determined as 0.04 $kJ.mm^{-1}$, and the shear critical fracture energies G_s^c and G_t^c is determined as 0.45 $kJ.mm^{-1}$. The material parameter is assumed to be 1.8 based on references [11,12]. The viscosity coefficient for the cohesive surface is assumed to be 0.001 s.

Compressive stress-strain relationship comparisons between numerical homogenization and experiments of unconfined steel reinforced resin are shown in Fig. 19. The macro scale stress is obtained based on Eq. (1), so the homogenization results are compared with true stress and strain relationship. A good agreement is observed, indicating it is reliable to use computational homogenization method to predict the tensile and shear behavior of steel reinforced resin. The uniaxial stress and strain relationship, shear stress and strain relationship based on numerical homogenization method is shown in Fig. 20. The ultimate tensile strength of steel reinforced resin is 39.8 Mpa. The mises stress distribution and deformation of the unit cell is shown in Figs. 21 and 22 at different stages in Fig. 20. The principal plastic strain at the failure of the unit cell is shown in Fig. 23. The numerical multiscale simulation indicated that the damage and failure of steel reinforced resin is governed by the resin and interface while the steel is in the elastic stage during uniaxial and shear loading. The friction angle β, the ratio of the yield stress in triaxial tension to the yield stress in triaxial compression K, and the dilation angle ψ are calculated based on Eqs. (34)–(40) and multiscale simulation results. The steel reinforced resin material parameters of the linear Drucker-Prager model are summarized in Table 8.

As is shown in Fig. 24, the unconfined steel reinforced resin compressive tests were simulated numerically using solid element C3D8R [18]. The uniaxial true stress and strain relationship and material parameters of the linear Drucker-Prager model are obtained based on multiscale simulation. The nominal stress-strain relationship of unconfined steel reinforced resin comparisons between finite element simulation and experimental results is shown in Fig. 25. A good agreement is observed.

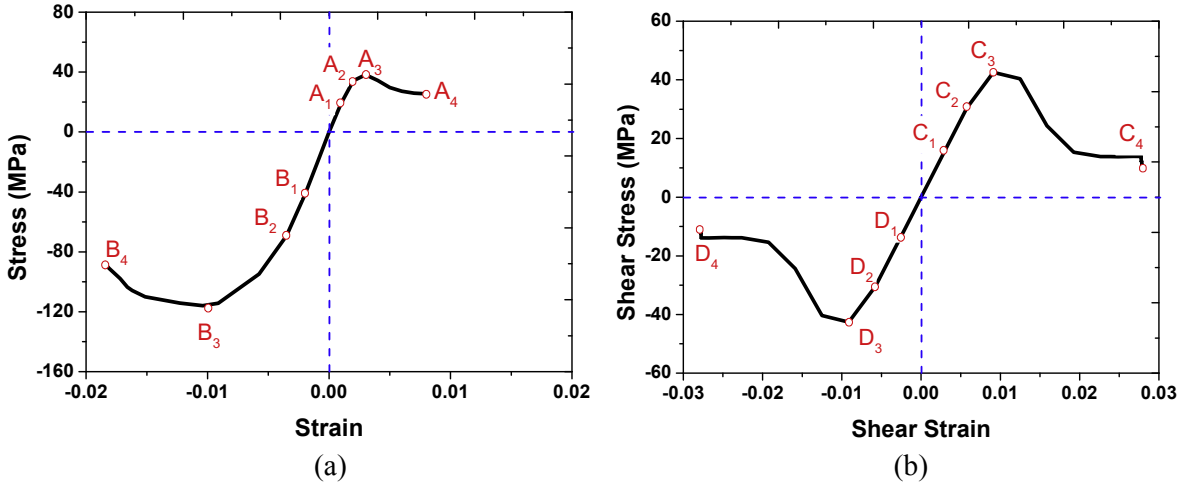

Fig. 20. Stress-strain relationship of steel reinforced resin from numerical homogenization.

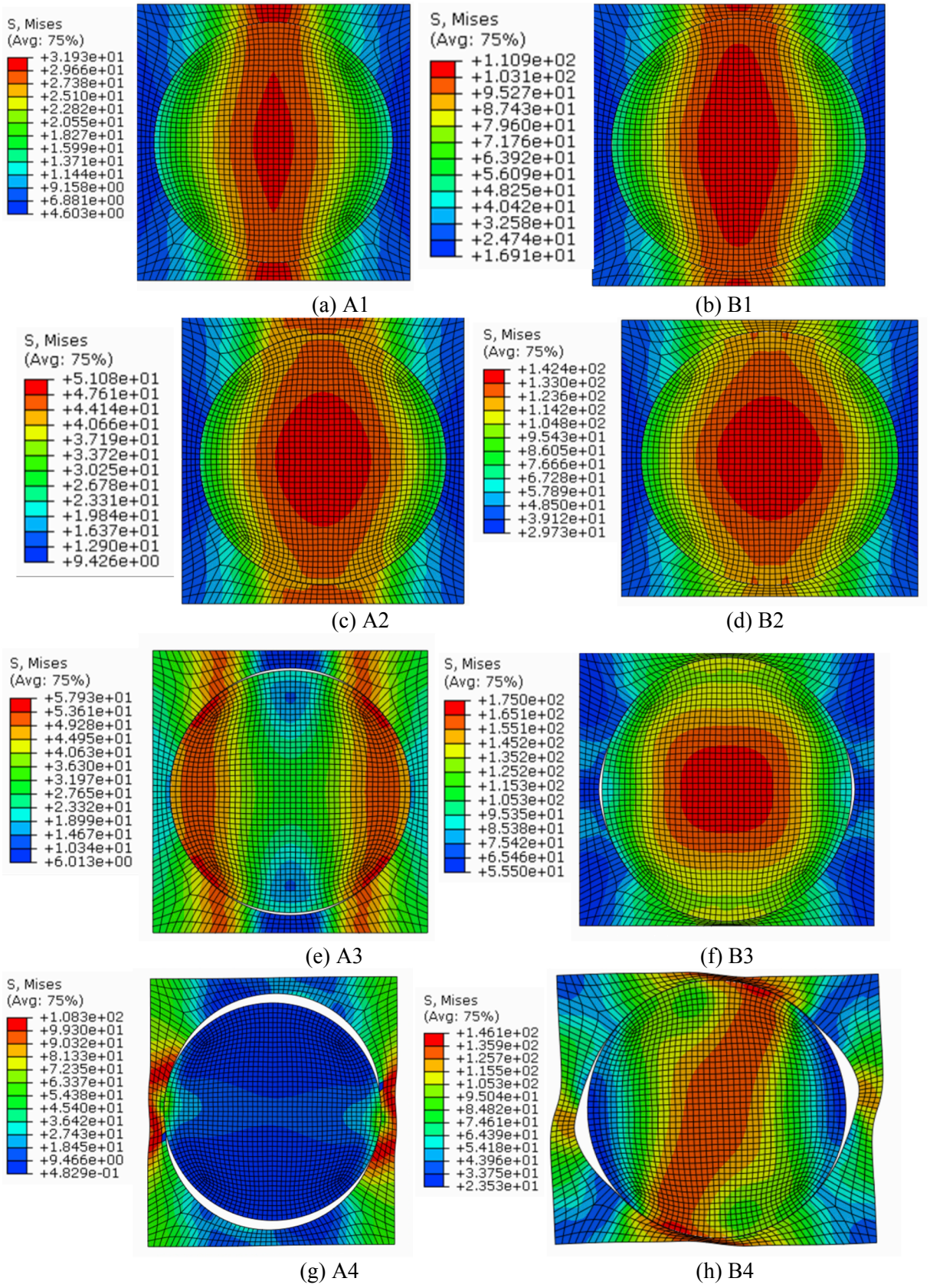

Fig. 21. Mises stress distribution of unit cell under unaxial loading.

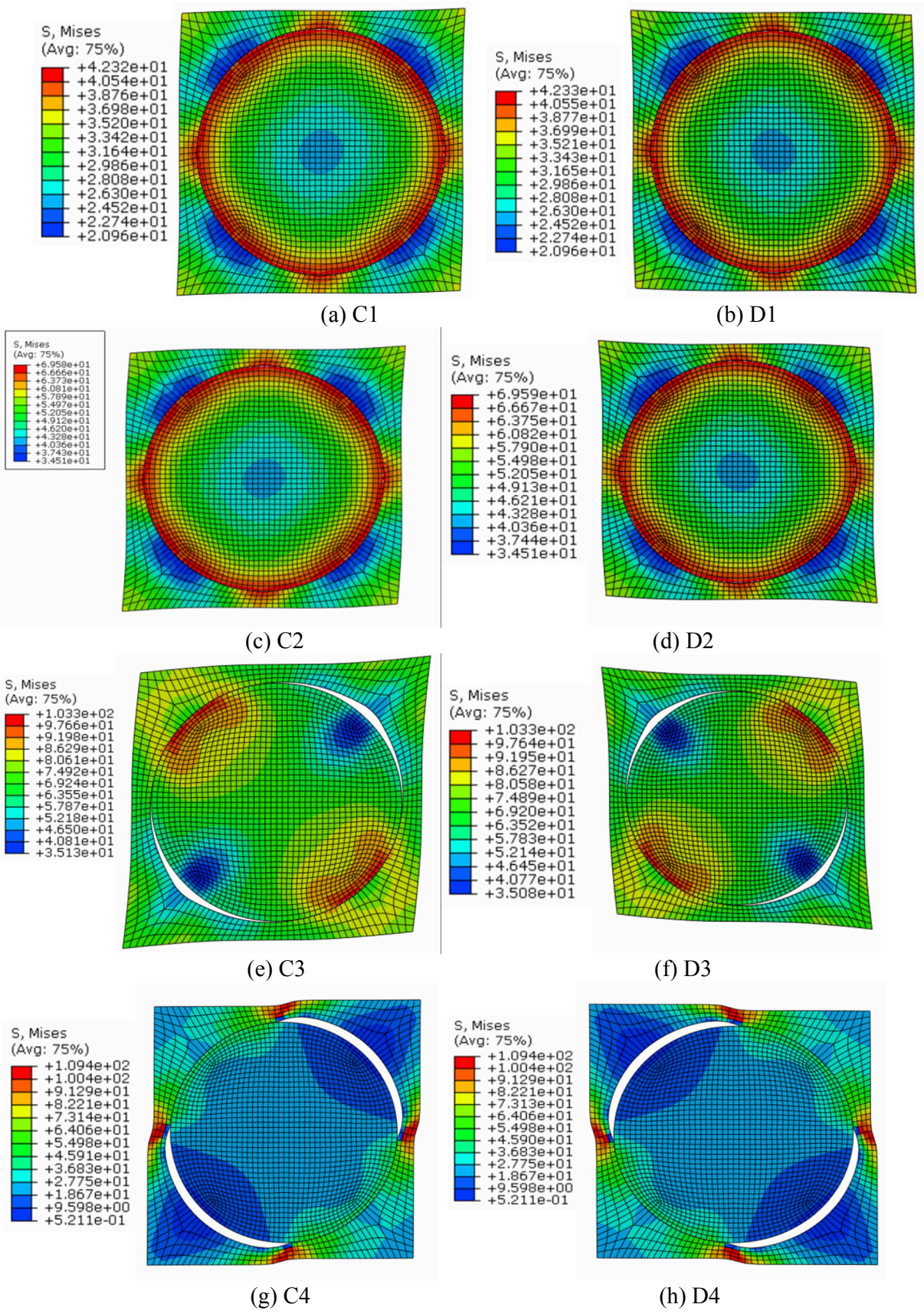

Fig. 22. Mises stress distribution of unit cell under shear loading.

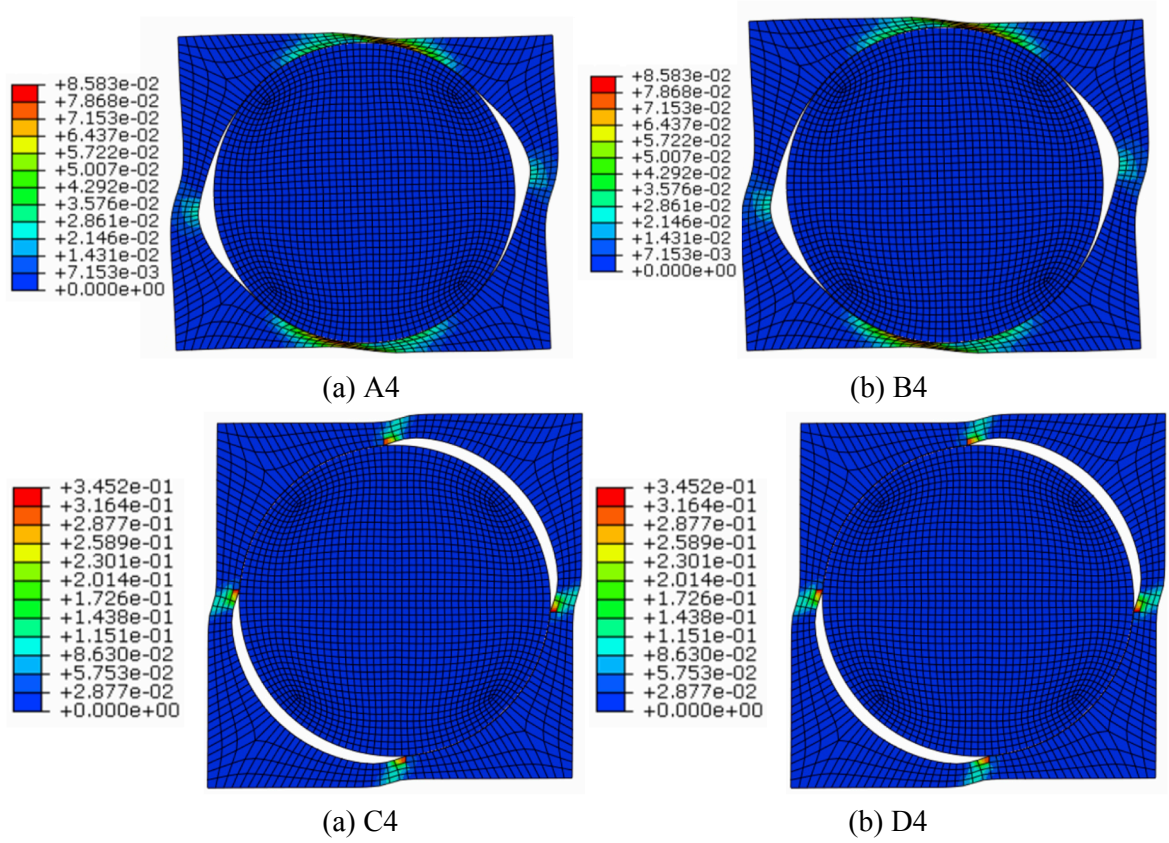

Fig. 23. Principal plastic strain of unit cell at failure.

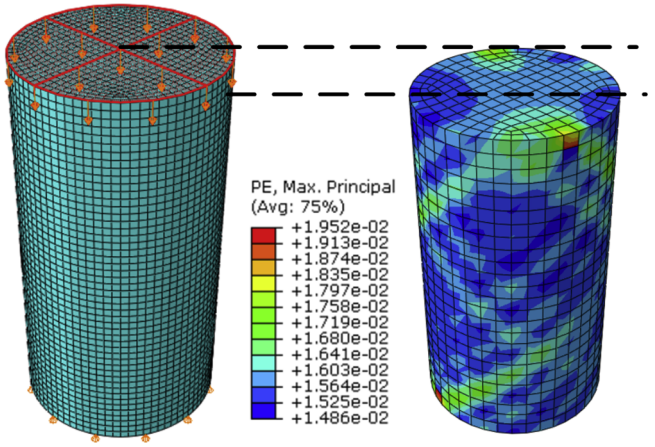

Fig. 24. Finite element model of unconfined steel reinforced resin specimen.

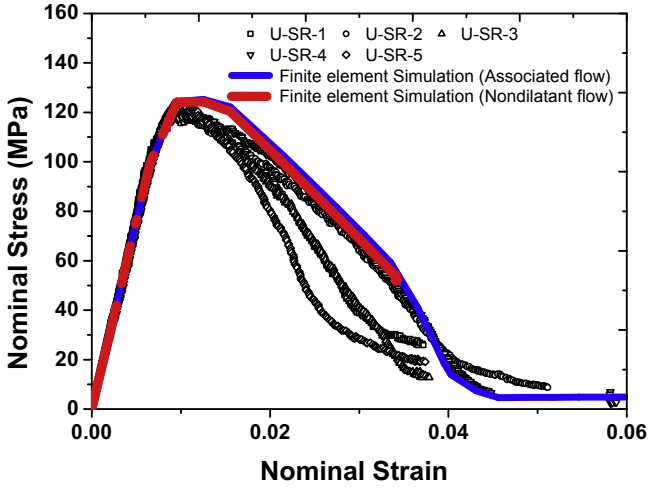

Fig. 25. Stress-strain relationship comparisons between FEM and experiments of unconfined steel reinforced resin.

5.2. Confined steel reinforced resin

Similar to confined resin tests, finite element model on confined steel reinforced resin tests was built to validate the efficiency of the linear Drucker-Prager model when predicting steel reinforced resin behavior with confinement. Same material model and parameter used in the unconfined steel reinforced resin simulation is employed during modeling confined tests. Same steel material model used in Section 4.2 is employed during modeling confined steel reinforced resin tests. The nominal stress-strain of confined steel reinforced resin comparisons between finite element simulation and experimental reuslts is shown in

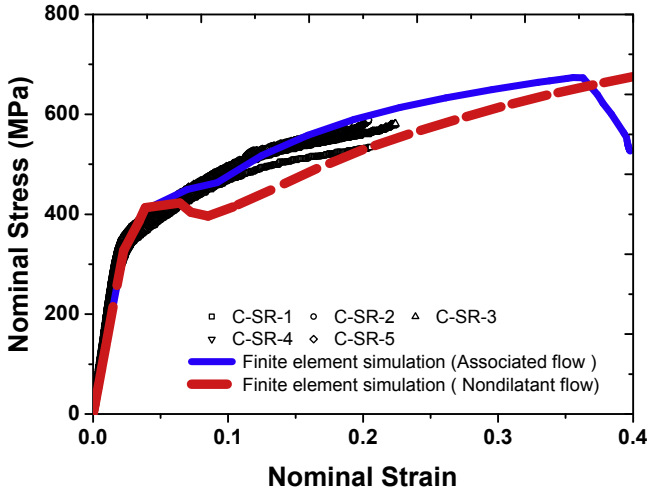

Fig. 26. Stress-strain relationship comparisons between FEM and experiments of confined steel reinforced resin.

Fig. 26. The finite element simulation results from "associated flow" model agreed well with the experimental results, but the simulation finite element simulation results from "nondilatant flow" tended to be smaller than the experimental results in the hardening stages. The Drucker-Prager models with "associated flow" rules could predict the confinement effects of steel reinforced resin efficiently. Fig. 27 showed deformation comparisons of confined steel reinforced resin tests between FEM and experiments. A good agreement is observed.

6. Conclusions

Compressive material tests on unconfined/confined resin and steel reinforced resin were experimentally evaluated in order to validate the numerical results. Finite element simulation and multiscale homogenization methods were successfully used in this study to effectively model the material properties of resin and steel reinforced resin. Based on the results of this study, the following conclusions are drawn:

(1) A combined damage mechanics and Ramberg-Osgood Relationship is proposed in this paper to describe the uniaxial compressive behavior of resin and steel reinforced resin. Related material parameters were fitted based on experimental results. The proposed uniaxial compressive model could effectively describe the uniaxial hardening/softening behavior of resin and steel reinforced resin during finite element simulation.

(2) Numerical homogenization is necessary for an accurate prediction of the non-linear behavior of steel reinforced resin in the situation that tensile and shear experiments are difficult to be conducted. A multiscale computational homogenization simulation is conducted to predict the tensile and shear behavior, Combined non-linear isotropic/kinematic cyclic hardening model is employed to define the steel plasticity, the linear Drucker-Prager plastic criterion was used to simulate resin damage. The cohesive surfaces, reflecting the relationship between traction and displacement at the interface, were employed to simulate the steel-resin interface. A good correlation between numerical homogenization results and test results was achieved. The damage of steel reinforced resin is mainly due to the plasticity of resin and interface damage.

(3) The friction angle , the ratio of the yield stress in triaxial tension to the yield stress in triaxial compression K, and the dilation angle ψ of the linear Drucker-Prager plastic model are obtained based on experiments and numerical homogenization to efficiently consider the confinment effects on resin and steel reinforced resin. The confinement effects on resin and steel reinforced resin could be effectively simulated by combing above parameters and uniaxial compressive model. Finite element simulations on unconfined/ confined resin and steel reinforced resin material tests were conducted to validate the linear Drucker-Prager plastic model and material parameters proposed in this paper. A good agreement is observed, indicating the model and parameters proposed in this paper could be effectively used in the numerical simulation of injected bolted connections.

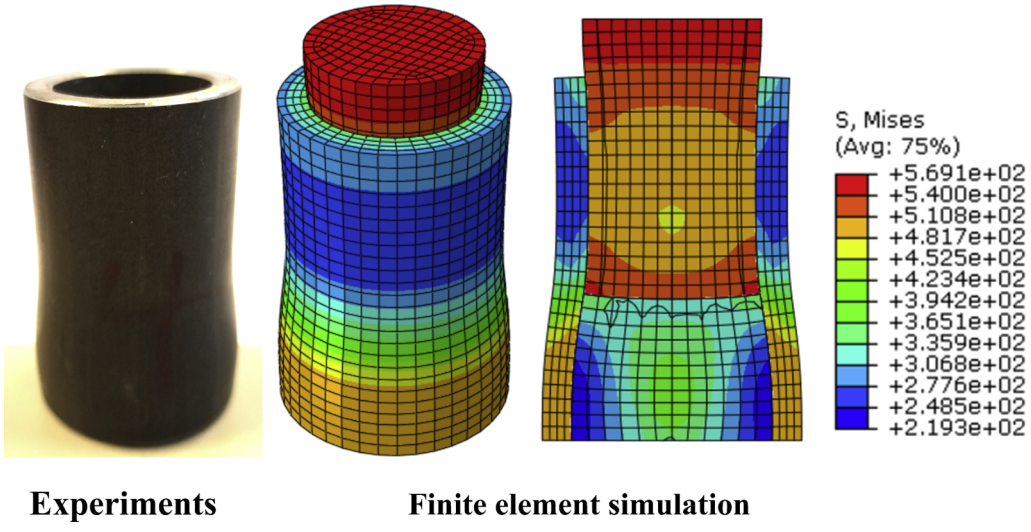

Fig. 27. Deformation comparisons between FEM and experiments of confined steel reinforced resin.

Acknowledgment

This research was carried out under project number T16045 in the framework of the Research Program of the Materials innovation institute (M2i) (www.m2i.nl) supported by the Dutch government.

References

[1] Nijgh MP, Xin H, Veljkovic M. Non-linear hybrid homogenization method for steel-reinforced resin. Constr Build Mater 2018;182:324–33.
[2] de Oliveira Correia JAF, Pedrosa BAS, Raposo PC, DeJesus AMP, dos Santos Gervásio HM, Lesiuk GS, et al. Fatigue Strength Evaluation of Resin-Injected Bolted Connections Using Statistical Analysis. Engineering 2017.
[3] Kolstein H, Li J, Koper A, Gard W, Nijgh M, Veljkovic M. Behaviour of double shear connections with injection bolts. Steel Constr 2017;10:287–94.
[4] Nijgh MP. New Materials for Injected Bolted Connections-A feasibility study for demountable connections. Delft University of Technology; 2017.
[5] Fish J. Practical multiscaling. John Wiley & Sons; 2013.
[6] Tal D, Fish J. Stochastic multiscale modeling and simulation framework for concrete. Cem Concr Compos 2018;90:61–81.
[7] Xin H, Sun S, Fish J. A surrogate modeling approach for additive-manufactured materials[J]. Int J Multiscale Comput Eng 2017;6:525–43.
[8] Xin H, Sun W, Fish J. Discrete element simulations of powder-bed sintering-based additive manufacturing. Int J Mech Sci 2018;149:373–92.
[9] Xin H, Mosallam AS, Liu Y, Wang C, He J. Experimental and numerical investigation on assessing local bearing behavior of a pultruded GFRP bridge deck. Compos Struct 2018;204:712–30.
[10] Xin H, Liu Y, Mosallam AS, He J, Du A. Evaluation on material behaviors of pultruded glass fiber reinforced polymer (GFRP) laminates. Compos Struct 2017;182:283–300.
[11] Xin H, Mosallam A, Liu Y, Xiao Y, He J, Wang C, et al. Experimental and numerical investigation on in-plane compression and shear performance of a pultruded GFRP composite bridge deck. Compos Struct 2017;180:914–32.
[12] Xin H, Mosallam A, Liu Y, Wang C, Zhang Y. Analytical and experimental evaluation of flexural behavior of FRP pultruded composite profiles for bridge deck structural design. Constr Build Mater 2017;150:123–49.
[13] Romanowicz M. A numerical approach for predicting the failure locus of fiber reinforced composites under combined transverse compression and axial tension. Comput Mater Sci 2012;51:7–12. https://doi.org/10.1016/j.commatsci.2011.07.039.
[14] Vaughan TJ, Mccarthy CT. Micromechanical modelling of the transverse damage behaviour in fibre reinforced composites. Compos Sci Technol 2011;71:388–96. https://doi.org/10.1016/j.compscitech.2010.12.006.
[15] Liu Y, Sun W, Fish J. Determining material parameters for critical state plasticity models based on multilevel extended digital database. J Appl Mech 2016;83:11003.
[16] Fish J, Yuan Z, Kumar R. Computational certification under limited experiments. Int J Numer Methods Eng 2018;114:172–95.
[17] Fish J, Fan R. Mathematical homogenization of nonperiodic heterogeneous media subjected to large deformation transient loading 2008:1044–64. https://doi.org/10.1002/nme.
[18] Abaqus V. 6.14 Documentation. Dassault Syst Simulia Corp 2014.
[19] EN1993-1-1. Eurocode 3: Design of steel structures – Part 1.1: General rules – General rules and rules for buildings. Brussels CEN 2005.
[20] Benzeggagh ML, Kenane M. Measurement of mixed-mode delamination fracture toughness of unidirectional glass/epoxy composites with mixed-mode bending apparatus. Compos Sci Technol 1996;56:439–49.
[21] Wedekamper FJ. Avaliação De resinas epóxi para aplicação em end fittings de dutos flexíveis. Universidade federal do rio grande do sul; 2017.
[22] Ramberg W, Osgood WR. Description of stress-strain curves by three. parameters 1943.